Article

Journal of
Nanoscience and Nanotechnology
Vol. 17, 6210–6215, 2017
www.aspbs.com/jnn

The *In Situ* Lattice Distortion Study on Relaxor PMN-PT Single-Crystal Under External Loading

Chengping Zhang[1,2], Zhiqiang Chen[2,*], and Yu Deng[1,*]

[1] *School of Physics, Modern Analysis Center, Nanjing University, Nanjing 210093, P. R. China*
[2] *Center for High Pressure Science and Technology Advanced Research, Shanghai 201203, P. R. China*

Transmission electron microscope (TEM) equipped with *in situ* loading systems such as the pressure and thermal ones, is powerful tool in geological research as well as in materials science. The nano-sized grain, domain microstructures and the local lattice distortion inside the complex compositions can be directly traced under variety of external loading, which is utilized to reconstruct the geological environment. Here we selected the relaxor $PbMg_{1/3}Nb_{2/3}O_3$-$xPbTiO_3$ (PMN-PT) single crystal as the model sample, performing atomic resolution observations on the complicated local domain structures and lattice distortions, under both mechanical and bias loading in the *in situ* TEM. We found that the splitting domain boundaries induced by the external fields, actually accommodate miniaturized unit-cell-size domains, instead of being simple domain walls. The unique domain splitting mechanism has been discussed.

Keywords: *In Situ* TEM, Lattice Distortion, Single-Crystal, Domain Boundary.

1. INTRODUCTION

TEM becomes more and more valuable in studying the microstructures from the fields of bionics and geography. Particularly, the recent development of the *in situ* TEM techniques makes it possible to trace many evolutions at atomic scale under heating, stress, electric field and chemical reaction environments.[1,2] For example, some natural rocks with exactly same composition and density however show great difference in hardness and brittleness.[3] Here the microstructures and the way they assemble play the key roles. Therefore, the TEM investigation provides a powerful tool to directly observe and analysis these complex microstructures.[4] Moreover, *in situ* TEM technique is also an attractive way. to reconstruct the similar geological environment (e.g., high pressure and temperature) and understand the geographic processes mechanism of the nanometer minerals.

Complex metal oxide PMN-PT single crystal can be mainly classified as the multifunctional materials of electrostrictive, photostrictive, shape memory and piezoelectric applications. The domain evolutions and local lattice strain/distortion are corresponding to the ultra large nonlinear strains.[5,6] And the morphotropic phase boundary also greatly contributes to the giant electro-mechanical response.[5–9] For past decades, the complicated phase structures (besides classic tetragonal, orthorhombic and the rhombohedral phases, there are three types of intermediary monoclinic phases between the tetragonal and orthorhombic, the orthorhombic and rhombohedral, the tetragonal and rhombohedral, respectively[10]) have been extensively studied by the X-ray, neutron diffraction, polarized-light optical microscopy and TEM. However, there are long time controversial on PMN-PT's local phase, domain and lattice distortion evolutions due to the complexity of the materials.[6–12] To understand these "hopeless mess"[11–14] relaxor behaviors, the direct observation on the electromechanical/mechanical response process at atomic resolution is needed. It's helpful to find the dominant response mechanism under a certain condition. Here, we studied the local domain and lattice structures of the ion-beam-thinned single-crystal PMN-PT by using an *in situ* TEM equipped with both bias and stress loading. The corresponding response processes were studied by high resolution TEM observations and Selected area electron diffraction (SAED).

*Authors to whom correspondence should be addressed.

 1533-4880/2017/17/6210/006 doi:10.1166/jnn.2017.14515

2. EXPERIMENTAL PROCEDURE

Commercially available PMN-PT single crystal (Shanghai Xikasi. Co.) is used in this work. X-ray diffraction experiments indicate that the macroscopic phase of the present crystals would be a tetragonal one.[11] We selected a [001] oriented PMN-PT slice from a bulk crystal. The specimen was mechanically thinned below 40 μm by diamond polishing discs before bonding to the *in-situ* Mo TEM grid which also acts as the bottom electrode. The slice was then Ar-ion milled at 5 kV and 80 uA with a 5° incident angle for 2 h, on a Gatan Precision Ion Polishing System (type II). The selected thin regions for this study are of average thickness of 25 nm. The *in situ* TEM observations were carried out on a JEOL 3010F TEM at 300 kV acceleration voltage. A Hysitron ECR in situ holder was used, with its doped diamond indentation tip of the holder being of good conductivity.

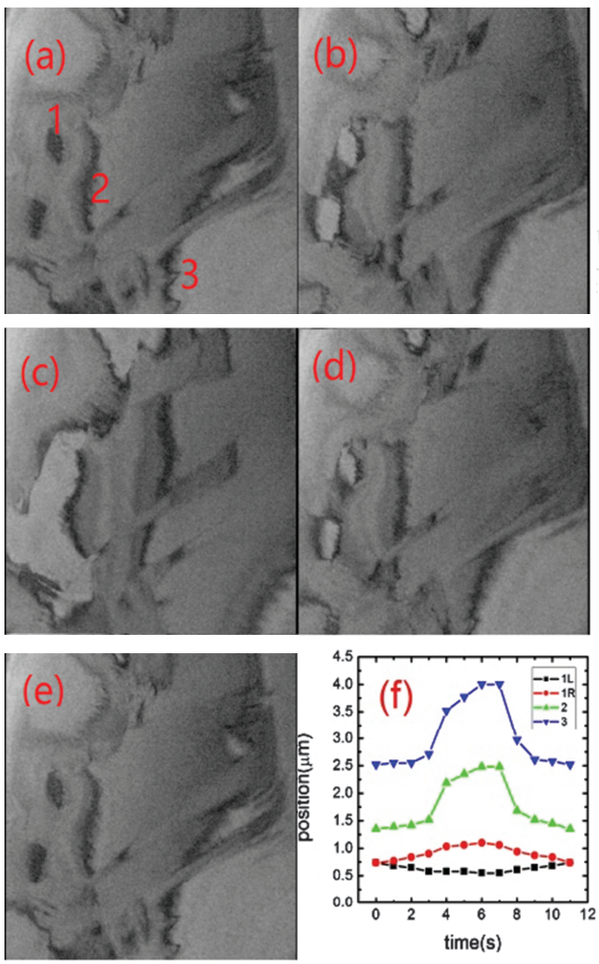

Figure 1. Electric field of the value of 0.5 V/μm is applied at the time of 0 s and turned off at the time of 6 s. (a∼e) show the motion of the domain boundaries, they are taken at the time of 0 s, 3 s 6 s, 8 s and 11 s, separately. (f) shows how the positions of the domain boundaries change with time.

3. *IN-SITU* TEM STUDIES ON BOUNDARY MOVEMENT

3.1. Boundary Movement Under Applied Electric Fields

Figures 1(a)∼(e) show how the domain boundaries move when the electric field turned on and turned off. Figure 1(f) shows how the positions of the domain boundaries change with time. The positions of the boundaries are determined by the distances between the boundaries and the left margins of the images. Black and red lines represent the left and the right boundary of the domain labelled as "1", while green and blue lines represent the boundaries labelled as "2" and "3".

The electric field is turned on at the time of 0 s, but the displacements of boundaries are very small before the time of 3 s. Then it took them about another 3 seconds to reach the limitation. The process is similar when the electric field is turned off. The reacting time of the domain boundaries is really long, compared with previous researches (nanoseconds).[6]

3.2. Boundary Movement Under Applied Pressure

A tip is used to apply pressure to the sample. The initial distance between the tip and the sample is 350 nm.

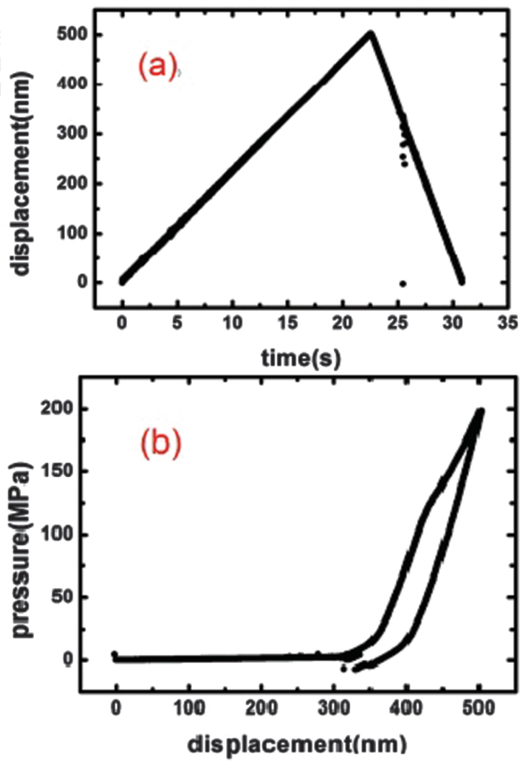

Figure 2. (a) The motion of the tip, it's moving toward the sample between 0∼22.5 s, and backward between 22.5∼30 s. (b) The pressure in sample. The initial distance between the tip and the sample is about 350 nm, hence when the displacement goes above 350 nm, the sample gets touched and the pressure increases rapidly.

The tip moves toward the sample between 0∼22.5 s, and backward between 22.5∼30 s, as shown in Figure 2(a). The tip touches the sample when the displacement reaches 350 nm, and then the pressure increases rapidly. The maximum of the displacement is 500 nm and the pressure reaches its maximum of 200 MPa at the same time.

Figure 3 shows dark field images taken between 15∼22 s, showing how the domain boundaries move, during the whole process which begins at 15 s, the time that the sample just gets touched by the tip, and ends at 22 s, the time that the pressure reaches its maximum.

The positions of the domain boundaries in the images can be determined and the speed of the movement of the boundaries can be calculated. Figure 4(a) shows the displacement of the boundaries. It can be roughly considered that the speed of the two boundaries is close and little changed with time. Figure 4(b) shows the angles made by the domain boundaries and the horizon. The angle does not change a lot in general, but they still have a tendency to become parallel. The tendency can also be seen in Figure 3.

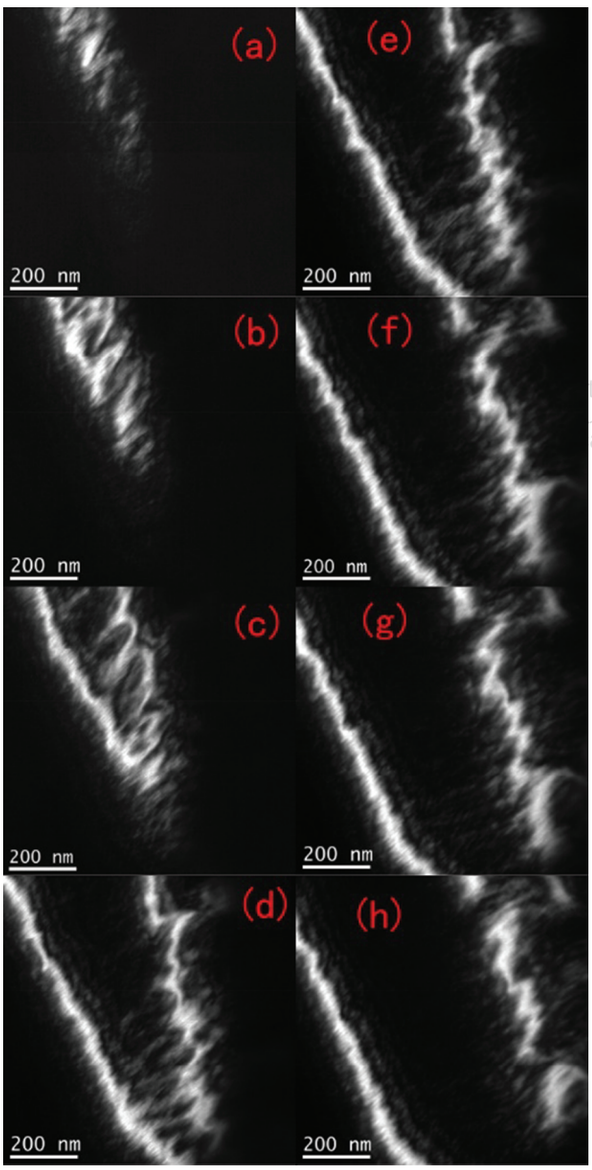

Figure 3. Dark field images taken between 15∼22 s, with the time interval of one second, show how the domain boundaries move during the process. The scale bar in each image is 100 nm.

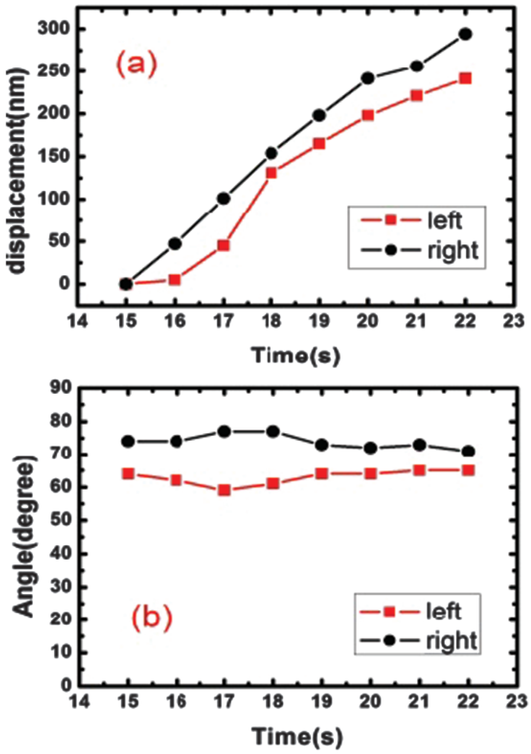

Figure 4. (a) shows the displacements of the domain boundaries. (b) Shows the angles made by the domain boundaries and the horizon.

The displacement of the left and the right boundary is 240 nm and 290 nm, respectively, during the whole 7 s, which means the average speed of the boundaries is 34 nm/s and 41 nm/s. And the average angles are 63° and 74°, makes the angle between the two boundaries about 11°.

4. TEM AND SAED RESULTS ON DOMAIN BOUNDARIES

4.1. Diffraction Patterns and Dark Field Images

Here, we found all the stable domain boundary state, i.e., before loading or after the electric/mechanical loading reaching its balance point, show some typical characters in common. Firstly, SAED is used to investigate the properties of the domain boundaries. Deviations of diffraction points are observed (Fig. 5), showing some interesting properties:

(1) The separations of the diffraction points reach maximum in $(\bar{1}0\bar{1})$ direction but the diffraction points in $(10\bar{1})$ direction do not split.

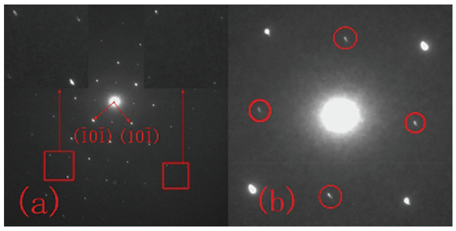

Figure 5. Diffraction pattern of PMN-0.33PT. (a) The separations of the diffraction points reach maximum in $(\bar{1}0\bar{1})$ direction but the diffraction points in $(10\bar{1})$ direction do not split. (b) All the separations are heading to the same direction.

(2) For those diffraction points that split, the separation is always along the $(\bar{1}01)$ direction.

4.2. Explanation of the Properties of the Deviations of Diffraction Points

The deviation of diffraction points is due to the difference in a and c in tetragonal phase. For tetragonal lattice, as shown in Figure 6, c is a little larger than a, which makes the reciprocal lattice, c^* a little smaller than a^*, due to the following relationship:

$$c^* = \frac{2\pi}{c} \quad a^* = \frac{2\pi}{a}$$

When there is a coexistence of two kind of lattices, the reciprocal lattices will be expected to overlap, as shown in Figure 7. There will be a small deviation of the diffraction points. Δg_{100} will be expected to be along the $(\bar{1}00)$ direction and Δg_{001} will be along the (001) direction.

Figure 5(b) shows that all the deviations are along the $(10\bar{1})$ direction.

This phenomenon can be explained if we take the tilt of the lattice into account. As c is a little bit larger than a, the angle β, which is made by the domain wall and the

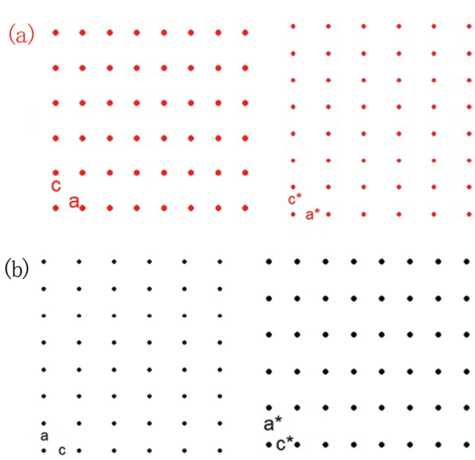

Figure 6. Tetragonal lattices with two different orientations and their corresponding reciprocal lattices.

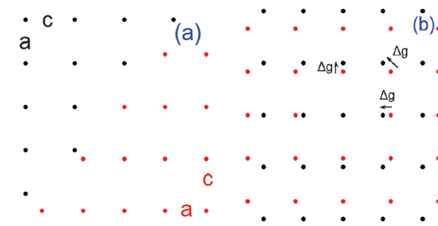

Figure 7. (a) Shows a coexistence of lattices with different orientations. (b) Shows the coexistence of two sets of diffraction patterns with a small deviation.

horizon, is also a little bit larger than 45°, and its theoretical value is:

$$\beta = \arctan\frac{c}{a}$$

This will result in a relative tilt of the lattice of the left upper domain, as shown in Figure 8(a). The angle of tilt, θ, can be determined as:

$$\theta = 2\beta - 90^\circ = 90^\circ - 2\arctan\frac{a}{c}$$

Correspondingly, there will also be a tilt, with the angle of θ, in the diffraction pattern, as shown in Figure 8(b). We can see that even though the angle of tilt is small, it will have a dramatic influence on the deviation Δg. All the deviations Δg are pointing to the same direction, which matches with the results of electron diffraction (Fig. 5(b)). Moreover, the deviations of the diffraction points along $(10\bar{1})$ direction are enlarged while the deviations of the diffraction points along $(\bar{1}01)$ direction disappear, this explains Figure 5(a). All these results can be proved mathematically.

First of all, let us consider the simplest case, the deviation of the diffraction point at (100), which is illustrated by Figure 9(a). Then

$$\Delta g_x = c^*\cos\theta - a^*$$

$$\Delta g_y = c^*\sin\theta$$

this can be simplified as:

$$\Delta g_x = -a^*\frac{c^2-a^2}{a^2+c^2}$$

$$\Delta g_y = c^*\frac{c^2-a^2}{a^2+c^2}$$

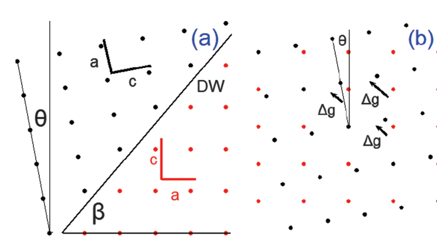

Figure 8. (a) The lattices near the 90° domain wall, there will be a tilt of θ between two sets of lattices. (b) The tilt of θ between two sets of diffraction patterns results in all the deviations of the diffraction points, Δg, to be parallel.

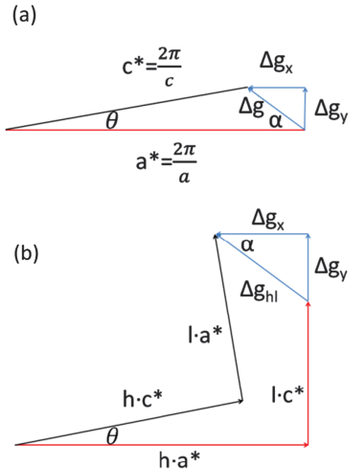

Figure 9. (a) Analysis of the deviation of diffraction points at (100). (b) Analysis of the deviation of diffraction points labelled by (h, l).

Then we have:

$$\alpha = \arctan\left|\frac{\Delta g_y}{\Delta g_x}\right| = \arctan\frac{a}{c}$$

$$|\Delta g| = |\Delta g_x^2 + \Delta g_y^2| = 2\pi\frac{c^2 - a^2}{ac\sqrt{a^2 + c^2}}$$

We can see that $\alpha + \beta = 90°$, which means the direction of Δg is perpendicular to the direction of the domain wall.

Now, let's consider the most general situation, the deviation of diffraction points at (h, l). The diffraction point of the right lower domain will be located at ($h \cdot a^*$, $l \cdot c^*$), while the diffraction point of the left upper domain will be located at ($h \cdot c^*$, $l \cdot a^*$) if there was no tilt. Take the tilt into consideration, the coordinate will be

$$(h \cdot c^* \cos\theta - l \cdot a^* \sin\theta,\ h \cdot c^* \sin\theta + l \cdot a^* \cos\theta)$$

Then we have

$$\Delta g_{x,hl} = h \cdot c^* \cos\theta - l \cdot a^* \sin\theta - h \cdot a^*$$

$$\Delta g_{y,hl} = h \cdot c^* \sin\theta + l \cdot a^* \cos\theta - l \cdot c^*$$

Which can also be simplified as

$$\Delta g_{x,hl} = -(h + l)a^*\frac{c^2 - a^2}{a^2 + c^2}$$

$$\Delta g_{y,hl} = (h + l)c^*\frac{c^2 - a^2}{a^2 + c^2}$$

Similarly we get

$$\alpha = \arctan\left|\frac{\Delta g_{y,hl}}{\Delta g_{x,hl}}\right| = \arctan\frac{a}{c}$$

$$|\Delta g_{hl}| = |\Delta g_{x,hl}^2 + \Delta g_{y,hl}^2| = 2\pi|h + l|\frac{c^2 - a^2}{ac\sqrt{a^2 + c^2}}$$

Surprisingly, the angle α is irrelevant with h and l, which means for all the diffraction points, Δg_{hl} are all parallel, and all perpendicular to the domain wall. From the expression of Δg_{hl}, we can see when $l = -h$, Δg_{hl} will be zero, this explains why there is no deviation in $(\bar{1}01)$ direction in Figure 5(b). And when $l = h$, the deviation will be enlarged, this is the case in (101) direction.

In many cases, a and c is very close, which means $\delta = (c/a) - 1 \ll 1$. In this case,

$$\alpha = \arctan\frac{a}{c} \approx 45°$$

and the expression of Δg_{hl} can be simplified as

$$\frac{|\Delta g_{hl}|}{a^*} = \sqrt{2}|h + l|\delta$$

4.3. Diffraction Point Splits into 4 Pieces

There are also some diffraction points split into 4 pieces, as shown in Figure 10, and the reason should be multiple. The case happens for both the stabled boundaries and the intermediate boundary states under large electric/mechanical loading (e.g., under the electric field for 5 s and the pressure for 10 s), which will continue to change after a further creeping process under the loading (for 102∼103 s). And it could be due to the coexistence of domain walls of different orientations, and also could be the result of the coexistence of different phases.

Generally, the boundary movement shows a "balance" state and a "balance" end state, which has been described in 4.1. and 4.2. However, the electric/mechanical loading can introduce some intermediate (metastable) boundary states, which will last long time (but not permanent) before finally transfer into the stable (balance) state. And these intermediate states are related to the MPB or charged domain structures.

4.4. HRTEM Images

In order to learn the detailed structure of the domain boundary, high resolution TEM (HRTEM) experiments were carried out, as shown in Figure 11. It doesn't contain

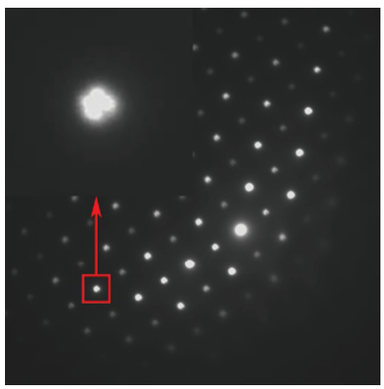

Figure 10. Diffraction point splits into 4 pieces.

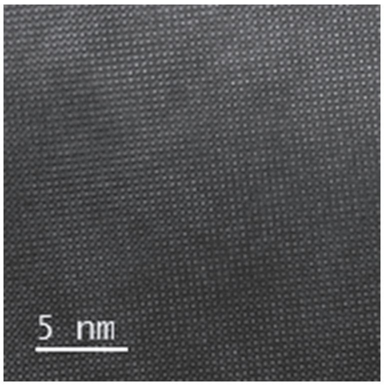

Figure 11. HRTEM images of domain boundaries, c/a is 1.005, very close to 1.

different kinds of polar directions as expected, but homogeneously distributed.

More, c/a is measured in a number of HRTEM images, and its average value is 1.005, smaller than the result from neutron diffraction,[5,15] which is 1.01.

5. CONCLUSIONS

PMN-PT single crystal has been traced at atomic resolution during the local domain evolutions induced by mechanical and bias loading. The miniature domain splitting at the initial domain boundaries has been detected, as well as the local lattice distortions. The unique behaviors of the domain boundaries are critical to the PMN-PT single crystal's electro-mechanical response. It greatly enhances the flexibility of the domain structures and the local phase transformations.

Acknowledgments: This work has been supported by the Natural Science Foundation of Jiangsu Province, China (Grant No. BK20151382), and the National Center for Electron Microscopy of Molecular Foundry at Lawrence Berkeley National Laboratory, for the support under the DOE Grant for user facilities.

References and Notes

1. Y. Sato, T. Hirayama, and Y. Ikuhara, *Phys. Rev. Lett.* 107, 187601 (**2011**).
2. K. H. Kim, D. A. Payne, and J. M. Zuo, *Appl. Phys. Lett.* 97, 261910 (**2010**).
3. J. C. Jaeger and N. G. W. Cook, Fundamental of Rock Mechanics, Chapman & Hall, London (**1969**)
4. A. G. Evans, Z. Suo, and R. Z. Wang, *J. Mater. Res.* 16, 2475 (**2001**).
5. L. E. Cross, *Ferroelectrics* 76, 241 (**1987**).
6. G. Catalan, J. Seidel, R. Ramesh, and J. F. Scott, *Rev. Modern Phys.* 84, 119 (**2012**).
7. M. Davis, *J. Electroceram.* 19, 25 (**2007**).
8. Z. G. Ye, B. Noheda, M. Dong, D. Cox, and G. Shirane, *Phys. Rev. B* 64, 184114 (**2001**).
9. B. Noheda, D. E. Cox, G. Shirane, J. Gao, and Z. G. Ye, *Phys. Rev. B* 66, 054104 (**2002**).
10. L. Kong, G. Liu, W. Yang, and W. Cao, *Appl. Phys. Lett.* 107, 042901 (**2015**).
11. A. K. Singh and D. Pandey, *Phys. Rev. B* 67, 064102 (**2003**).
12. G. S. Xu, H. S. Luo, H. Q. Xu, and Z. W. Yin, *Phys. Rev. B* 64, 020102 (**2001**).
13. J. M. Kiat, Y. Uesu, B. Dkhil, M. Matsuda, C. Malibert, and G. Calvarin, *Phys. Rev. B* 65, 064106 (**2002**).
14. H. Wang, J. Zhu, N. Lu, A. A. Bokov, Z. G. Ye, and X. W. Zhang, *Appl. Phys. Lett.* 89, 042908 (**2006**).
15. H. Wang, J. Zhu, X. W. Zhang, Y. X. Tang, and H. S. Luo, *J. Am. Ceram. Soc.* 91, 2382 (**2008**).

Received: 16 February 2016. Accepted: 12 September 2016.